Compact Antenna With Broadband Wireless Biotelemetry for Future Leadless Pacemakers

Abdulwahab Alghamdi, *Student Member, IEEE*, Abdul Basir, *Member, IEEE*, Amjad Iqbal, *Member, IEEE*, Roy B. V. B. Simorangkir, *Member, IEEE*, Muath Al-Hasan, *Senior Member, IEEE*, and Ismail Ben Mabrouk, *Senior Member, IEEE*

***Abstract*—This paper introduces a miniaturized implantable antenna designed to achieve ultra-wide bandwidth for next-generation leadless cardiac pacemakers (LCPs). A broad bandwidth is essential for mitigating detuning challenges and enhancing channel capacity to enable advanced features in LCPs. This antenna, with a volume of 9.44 mm³, achieves a bandwidth of 3.39 GHz and a fractional bandwidth (FBW) of 138%. The antenna covers various frequency bands from 0.76 to 4.15 GHz, including ISM (0.869, 0.915, and 2.45 GHz), WMTS (1.4 GHz), and midfield (1.6 GHz) bands. Antenna simulations conducted within a homogeneous phantom (HP) of heart tissue show gains of −32.4, −27.94, and −19.8 dBi at 0.915 GHz, 1.4 GHz, and 2.45 GHz, respectively. The proposed antenna exhibits low Specific Absorption Rate (SAR) levels within a full body model (FBM), achieving values of less than 1.6 W/kg and 2.0 W/kg for 1 g and 10 g of tissue, respectively. Furthermore, an analysis of the link budget is performed to calculate the telemetry range for a 10 Mbps data rate. The fabricated prototype is measured in minced pork meat, showing a good match with the simulation results.**

***Index Terms*—Implantable antenna, leadless cardiac pacemaker, ultra miniaturization, ultra-wide bandwidth.**

I. Introduction

In recent years, there has been a notable increase in the demand for miniaturized antennas in implantable medical devices (IMDs) for wireless biotelemetry. Among these devices, pacemakers play a crucial role in monitoring and regulating heartbeats. However, traditional pacemakers (TPs) face challenges associated with transvenous leads, which may result in complications such as infections. Recent studies indicate that approximately 1 out of every 14 patients experience lead-related complications, resulting in a mortality rate of 20% among those affected [1]. To address these issues, LCPs have been proposed as a solution for wireless pacing [2]. LCPs offer several advantages, including cost-effectiveness, reduced invasiveness, and improved efficiency. These devices are implanted directly into the heart, as illustrated in Fig. 1. Implantable antennas are critical components in wireless LCPs, enabling remote monitoring of patients by healthcare providers via smartphones and computers. However, designing compact antennas for LCPs is challenging due to the limited space available and the need for wideband performance. Deep tissue placement of LCPs poses significant challenges due to propagation losses in cardiac tissue that attenuate RF signals, requiring careful antenna design with optimal frequency selection and improved radiation efficiency. This challenge is compounded by variations in human tissue properties resulting from factors such as age or changes in the implantation site. Apart from mitigating frequency detuning caused by tissue variations, increasing the bandwidth of implantable antennas is crucial for improving channel capacity. A wider bandwidth allows for higher data rates, which are essential for enabling advanced features in LCPs. Future advancements in leadless pacing technology will likely require greater data transmission capabilities to support features like dynamic device programming and enhanced monitoring [3]. Ultra-wideband antennas optimize LCP battery life through intermittent data transmission, activating as needed. These features have the potential to significantly enhance the adaptability and improving patient outcomes. However, achieving a wide bandwidth while maintaining a compact antenna size remains a challenge in the design of implantable antennas for LCPs, as the miniaturization of antennas often comes at the cost of reduced bandwidth [4].

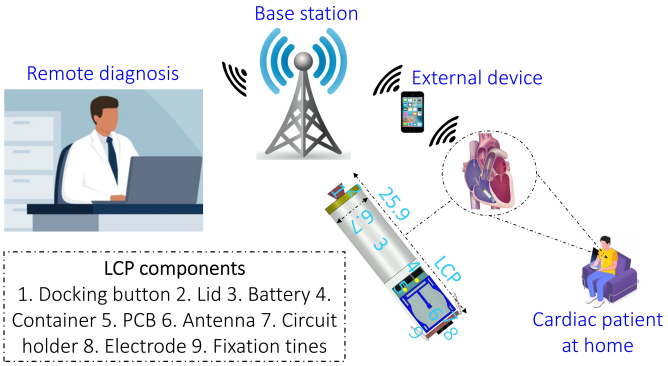

Fig. 1. Structure of the leadless cardiac pacemaker and its components.

Various implantable antenna designs have been proposed to achieve wide bandwidth while ensuring compact antenna size [5]–[11]. In [5], coupled small loop antennas are utilized to achieve a wide bandwidth of 74.1%. Capacitance loading techniques are employed in [7] to obtain a bandwidth of 20.5%. Similarly, metamaterials are used in [8] to achieve a wide bandwidth of 88.6%. The ground plane is truncated in [10] to attain a bandwidth of 40.8%. In another study [11], the authors utilized a spiral-shaped patch and a high permittivity substrate to achieve a bandwidth of 84% thanks to the inductive nature of the spiral structure. However, the antennas presented in [5], [7], [8], [10], [11] are not suitable for LCPs due to their larger dimensions compared to commercially available LCPs such as Nanostim (42 mm × 5.9 mm) and Micra (25.9 mm × 6.7 mm). More compact antenna designs have been reported in the literature, but they often suffer from narrow bandwidths. For instance, in [12], an antenna with a volume of 39.3 mm³ with a bandwidth of 14.9% was designed. Similarly, in [13], an antenna with dimensions of 24 mm³ and a bandwidth of 8.57% is introduced. In another study [14], the authors presented an antenna with dimensions of 17.15 mm³, operating at 2.45 GHz with a bandwidth of 9%. The authors in [15] presented a spiral-shaped antenna with a volume of 6 mm³, operating at 2.4 GHz and

Manuscript received 9 March 2024. (Corresponding author: Abdulwahab Alghamdi. This work was supported by the Royal Society under Newton International Fellowship (Grant Number: NIF\R1\221500). Abdulwahab Alghamdil, Amjad Iqbal, Roy B. V. B. Simorangkir, and Ismail Ben Mabrouk are with the Department of Engineering, Durham University, Durham DH1 3LE, U.K., Muath Al-Hasan is with the Department of Network and Communications Engineering, Al Ain University, UAE, Abdul Basir is with the Department of Engineering, Tampere University, Hervanta 33720 Tampere, Finland (e-mail: abdulwahab.alghamdi@durham.ac.uk; engrobasir@gmail.com; amjad730@gmail.com; roy.b.simorangkir@durham.ac.uk; ismail.benmabrouk@durham.ac.uk).

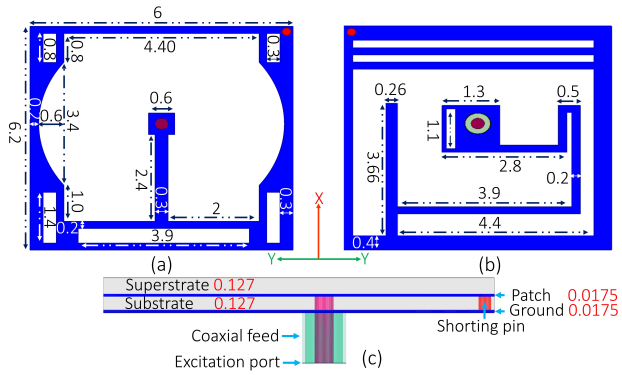

Fig. 2. Structure of the proposed implantable antenna, shown in (a) front, (b) back, and (c) side views (units: mm).

achieving a bandwidth of 21.8%. Finally, [16] introduced an antenna with a volume of 10.66 mm³ and a bandwidth of 131.6%, overcoming the issue of narrow bandwidth seen in other compact designs.

This study presents a novel implantable antenna specifically designed for next-generation leadless pacemakers to address the limitations of existing designs and bridge the gap between compact size and wide bandwidth. The proposed antenna achieves a compact volume of only 9.44 mm³, making it one of the smallest implantable antennas reported in the literature. Despite its miniature size, the antenna offers a significantly wider bandwidth of 138% compared to state-of-the-art designs. This enhanced bandwidth supports high-speed data transmission, advanced LCP functionalities [17], and resilience to detuning from tissue variability, ensuring reliable in-body communication. High-speed communication systems require wide bandwidths to achieve higher data rates. This relationship is described by the Shannon-Hartley theorem, as expressed in Equation (1) [18]:

$$C = B \times \log_2(1 + \text{SNR}) \tag{1}$$

where C represents the channel capacity (the maximum achievable data rate), B is the bandwidth, and SNR is the signal-to-noise ratio. A wideband antenna, having a larger bandwidth B, facilitates a higher channel capacity C, particularly when the signal-to-noise ratio (SNR) is sufficient. This performance is achieved through the incorporation of innovative design techniques, including expanded slots in the ground plane, a U-shaped slot, additional rectangular slots on the radiating patch, and an inductive shorting pin. To the best of our knowledge, the suggested antenna outperforms previously reported designs in terms of fractional bandwidth, as well as physical and guided wavelength size.

II. METHODOLOGY

A. Antenna Design

The complete geometric model of the suggested antenna, measuring 6.2 mm × 6 mm × 0.254 mm (9.44 mm³), is illustrated in Fig. 2. These dimensions ensure the antenna fits within a commercial leadless pacemaker. The radiating patch is rectangular in shape with a large U-shape slot at the center. An inductive shorting pin with a radius of 0.1 mm is positioned at one of the corners of the patch. Additionally, several rectangular slots are present on its edges as shown in Fig. 2(a). On the opposite side of the patch, a ground plane featuring a series of expanded slots is added, as illustrated in Fig. 2(b). Reactive loading techniques are employed to achieve wideband characteristics while maintaining the compactness of the antenna [19]. These design choices carefully consider deep tissue implementation needs, especially for leadless pacemaker applications, as detailed in the next subsection. The antenna employs Rogers RO3003 material, characterized by a tangent loss ($\tan\delta$) of 0.0010 and dielectric constant (ε_r) of 3. Both the substrate and superstrate have a thickness of 0.127 mm, adhering to the standard thickness of Rogers material. Fig. 2(c) presents a side view of the proposed antenna, which is fed via a coaxial feed with a characteristic impedance of 50 Ohms.

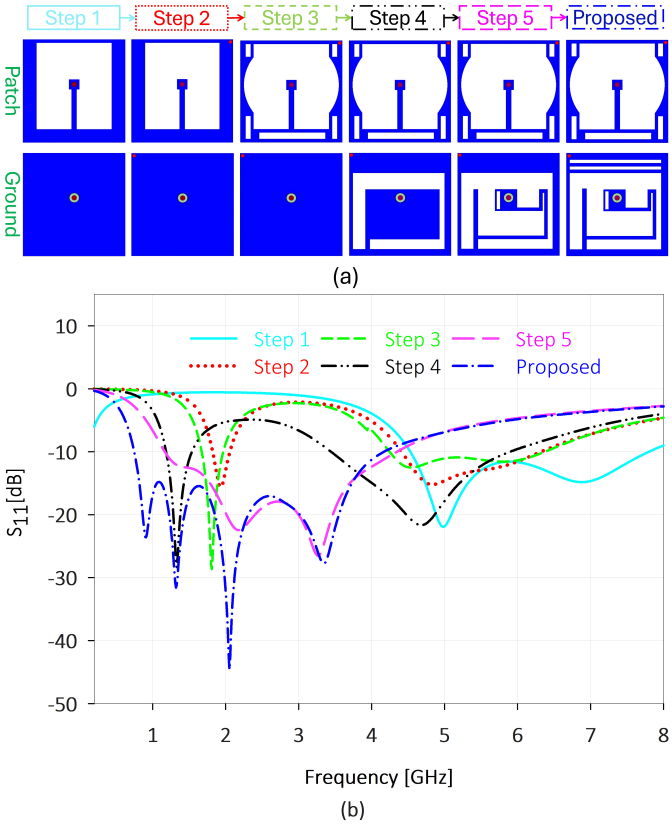

Fig. 3. (a) Evolution of design adjustments. (b) S_{11} reflection Coefficient at different design steps.

B. Parametric Study

Fig. 3(a) illustrates the design evolution of the proposed antenna structure, broken down into six steps. A comprehensive comparison of the reflection coefficient (S_{11}) is shown in Fig. 3(b). The primary aim of the proposed design is to achieve wide bandwidth while maintaining a compact size. In the first step, the design process begins with a rectangular patch antenna with a full ground plane, having a large U-shaped slot at the center and fed by a coaxial feed. The U-slot introduces capacitance and inductive loading, altering the electric field distribution and, through coupled-mode theory, creates resonant points to broaden the bandwidth [20]. This initial design exhibits a bandwidth ranging from 4.5 to 7.7 GHz. Moving to the second step, a shorting pin is introduced at the top right corner, connecting the patch to the ground plane. The ground plane remains complete in this step. The shorting pin functions as a lumped inductor, altering the current distribution and generating a new low-frequency resonance at approximately 1.95 GHz, leading to a dual-band response [21], [22]. However, the impedance matching at this new resonance is weak, leading to a narrowband resonance at 1.95 GHz. Proceeding to the third step, additional rectangular slots are added to the patch, i.e., one slot at the bottom and four slots at the corners of the radiating patch. In addition, the original U-shaped slot at the center of the patch is modified to include round cuts on both the left and right sides. These

TABLE I
DIELECTRIC PROPERTIES OF HEART AT VARIOUS FREQUENCIES

Phantom type	Frequency (GHz)	Conductivity (S/m)	Relative permittivity
HP	0.915	1.2378	59.796
	1.4	1.5132	57.538
	2.45	2.2561	54.814

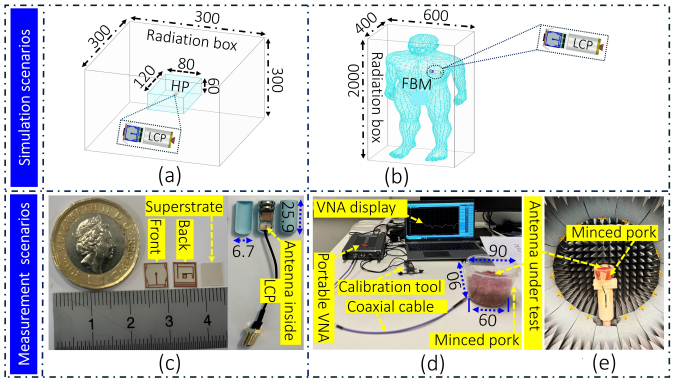

Fig. 4. (a) Homogeneous phantom (HP), (b) Full body model (FBM), (c) Fabricated prototypes, (d) Setup for S-parameter measurements, and (e) Setup for gain measurements (units: mm).

changes fine-tune resonant modes and increase capacitive loading, adding resonances and broadening impedance bandwidth through stagger-tuned resonance [23]. Each slot adds capacitance, disrupts current paths, and adjusts permittivity, enabling resonance control without increasing patch size. As a result, improved impedance matching of the first band and a slightly enhanced bandwidth of the second band are achieved. In the fourth step, a U-shaped slot is introduced in the ground plane, while the radiating patch remains unchanged from the previous step. This modification marks the beginning of a series of progressive expansions of the slot in the ground plane, which continues through the fifth and sixth steps. The introduction of the U-shaped slot enhances bandwidth by adding capacitive loading, which lowers the resonant frequency and improves impedance matching. It also enables the ground plane to contribute to radiation [24], enhancing overall antenna performance. As a result, the dual-band response is maintained, with the lower frequency band shifting by approximately 500 MHz and the higher frequency band by around 1.2 GHz, resulting in a wider bandwidth ranging from 3.43 to 5.8 GHz. The fifth step involves further expansion of the U-shaped slot in the ground plane, which modifies the effective dielectric constant of the antenna. This change lowers the resonant frequency and improves impedance matching across a broader frequency range. The impact on the antenna's performance is significant, as shown in the S11 plot (purple line). Consequently, the first and second frequency bands begin to merge, resulting in a wider bandwidth spanning from 1.17 to 4.34 GHz. Finally, in the sixth step (Proposed Antenna), two additional slots are etched on the top of the ground plane. These slots create new current paths that couple with existing resonant modes, enhancing impedance matching and broadening the bandwidth [25]. This distributed tuning of inductance and capacitance helps maintain stable resonance points under varying conditions and supports multi-band operation for reliable in-body medical telemetry. As a result, a wide bandwidth of 3.39 GHz is achieved, spanning from 0.76 GHz to 4.15 GHz, effectively covering the ISM bands (0.869 GHz, 0.915 GHz, and 2.45 GHz), WMTS (1.4 GHz), and the midfield band (1.6 GHz).

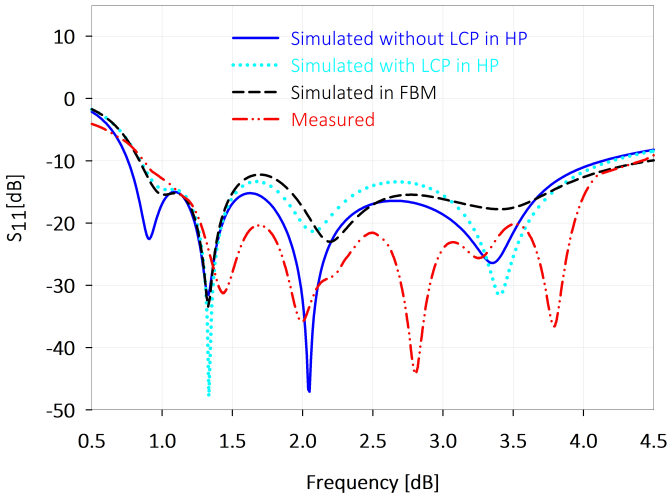

Fig. 5. S_{11} analysis of the proposed antenna under different scenarios, including with and without LCP.

C. Simulation and Measurement Configuration

The suggested antenna structure is simulated using the HFSS simulator. In the simulation, the antenna is integrated into an LCP designed as a capsule with dimensions of 25.9 mm in length and 6.7 mm in diameter, matching the dimensions of the commercial Micra pacemaker. The capsule has a thickness of 0.2 mm made of biocompatible ceramic alumina (Al_2O_3, ε_r = 9.8). Inside the pacemaker capsule, the antenna is positioned alongside a battery and associated dummy electronics. The implantable antenna is then placed at a depth of 30 mm in the center of a homogenous phantom (HP), as shown in Fig. 4(a). To mimic the dimensions of a typical human heart, the HP is designed with measurements of 120 mm $\times$ 80 mm $\times$ 60 mm, in accordance with guidelines from [26]. Moreover, the heart's electrical properties at target frequencies of 0.915, 1.4, and 2.45 GHz are appropriately assigned to the HP as shown in Table I [27]. These frequencies were selected for simulation and measurement due to their importance in biomedical applications: 915 MHz for ISM use, 1400 MHz for telemetry and communication, and 2450 MHz for wireless communication. Additionally, a radiation box is established, positioned at a distance greater than $\lambda_o/4$ from the antenna's edges [28]. Fig. 4(b) depicts the antenna implanted in a full-body model (FBM), approximately positioned at the heart location, providing a more realistic assessment of its performance. The antenna prototypes were fabricated and integrated within a 3D-printed leadless pacemaker capsule, along with dummy components, for experimental testing, as shown in Fig. 4(c). For testing, the LCP was placed at the center of a container filled with minced pork to measure the S-parameters using a Vector Network Analyzer (VNA) (Keysight P5004). The connections to the VNA ports were made using high-quality cables to ensure secure and accurate measurements, as shown in Fig. 4(d). The fabricated antenna was connected to the VNA, which was well-calibrated using known standards such as open, short, and load to correct for system errors like cable losses and connector mismatches. After calibration, the VNA was set to the desired frequency range. The radiation patterns were measured in a SATIMO anechoic chamber using a setup that included a signal generator powering a high-gain horn antenna as the transmitting antenna (Tx) and the proposed antenna as the receiving antenna

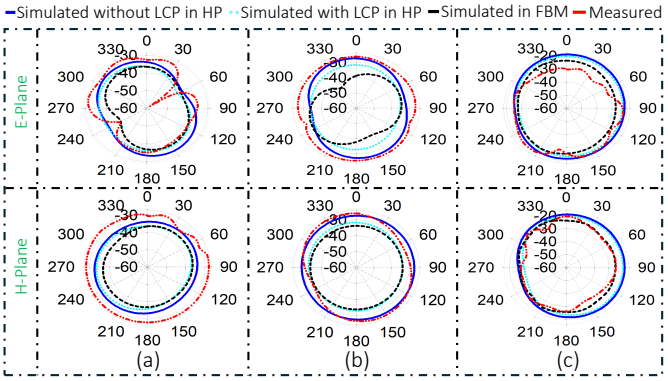

Fig. 6. Far-field patterns at frequencies of (a) 0.915 GHz, (b) 1.4 GHz, and (c) 2.45 GHz.

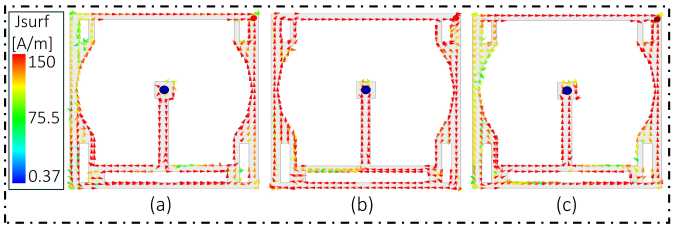

Fig. 7. Current distribution on the patch at frequencies of (a) 0.915 GHz, (b) 1.4 GHz, and (c) 2.45 GHz.

(Rx). A distance of 1 meter was maintained between the Tx and Rx antennas, as depicted in Fig. 4(e).

III. PERFORMANCE ANALYSIS AND DISCUSSION

The antenna's suitability for deep tissue implementation was assessed through comprehensive analyses, including simulations conducted in both a homogeneous phantom and a full-body model, followed by experimental validation using a tissue-mimicking medium.

A. Influences on Performance

Fig. 5 illustrates the comparison of S_{11} of the suggested antenna (with and without LCP) under various scenarios. The antenna demonstrates broad bandwidth and maintains good impedance matching across the desired frequency bands in all scenarios. The bandwidth of the proposed antenna is 3.39 GHz without LCP, 3.35 GHz with LCP, 3.55 GHz in the FBM, and 3.63 GHz during measurements. The measured S_{11} exhibits a wider bandwidth, likely due to variations in tissue properties. Additionally, a 0.5 GHz frequency shift between measured and simulated results is observed, likely caused by differences in the permittivity of minced pork versus human heart tissue, with estimated permittivity (48–50) and conductivity (0.6–2 S/m) affecting the shift.

B. Radiation Patterns

The radiation patterns of the suggested antenna are analyzed across different scenarios at 0.915, 1.4, and 2.45 GHz, as depicted in Fig. 6. The results exhibit omni-directional coverage. In the HP, the peak simulated gains without LCP are -32.4, -27.94, and -19.8 dBi at 0.915, 1.4, and 2.45 GHz, respectively. With LCP, gains are reduced to -34.6, -31, and -20 dBi. In the FBM, the maximum gains are -35.76, -32.01, and -22.06 dBi at the same frequencies. The measured gains are -29.3, -25.8, and -19.4 dBi, respectively. In fact, the gain of implantable antennas highly depends on the implantation depth [29]. In the measurements, the phantom size is smaller than what is used in the simulations. Therefore, the measured gain values are slightly higher than the simulated ones.

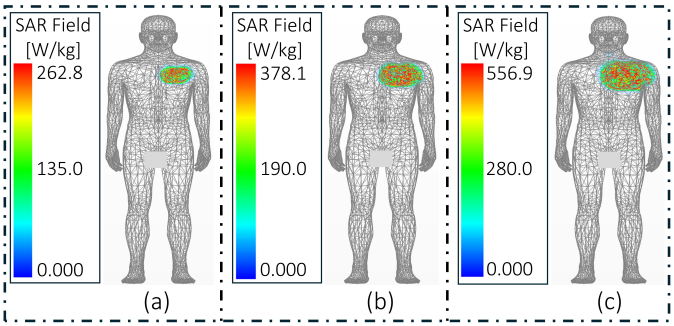

Fig. 8. SAR values at frequencies of (a) 0.915 GHz, (b) 1.4 GHz, and (c) 2.45 GHz.

TABLE II
MAXIMUM SAR AND MAXIMUM ALLOWABLE POWER

Phantom type	Frequency (GHz)	SAR W/kg (1g)	MAP (mW)	SAR W/kg (10g)	MAP (mW)
FBM	0.915	262.8	6.08	54.6	36.6
	1.4	378.1	4.23	40.3	49.6
	2.45	556.9	2.87	31.5	63.5

C. Surface Current Distributions

The current distributions across the antenna's patch at frequencies of 0.915, 1.4, and 2.45 GHz are illustrated in Fig. 7(a)–(c). In Fig. 7(a), a uniform flow of surface currents is observed on the radiating patch originating from the port, with the highest magnitude on the right side of the patch. In Fig. 7(b), the currents on the patch change direction along the port's line and near the shorting pin. At 1.4 GHz, the current path is longer than at 915 MHz because both the right and left sides of the patch have a strong concentration of current. Fig. 7(c) reveals that at 2.45 GHz, the currents behave similarly to those at 1.4 GHz, but with a shorter current path than the other two resonances. These currents flow along extended pathways on the patch, contributing to the antenna's compact size.

D. Specific Absorption Rate Distribution

SAR values must remain below 1.6 W/kg and 2 W/kg for 1 and 10 grams of tissues, respectively [30]. The SAR levels within the FBM and Maximum Allowed Power (MAP) are assessed. In simulations, the input power was initially set at 1 W to facilitate comparison with recent studies. This resulted in SAR values exceeding the safety limits: over 1.6 W/kg for 1 gram of tissue and over 2 W/kg for 10 grams of tissue. Fig. 8(a)–(c) illustrates SAR at frequencies of 0.915, 1.4, and 2.45 GHz. The highest SAR value over 1 gram of tissues recorded is 556.9 W/kg at a frequency of 2.45 GHz, with a MAP of 2.87 mW. To ensure safety, -16 dBm was chosen as the maximum allowable input power according to European Research Council regulations [31]. This level meets SAR compliance and reduces electromagnetic interference (EMI) with nearby wireless devices, preventing disruptions in multi-device environments and ensuring regulatory adherence. Table II shows the SAR and MAP values for the antenna. However, when the input power was adjusted to -16 dBm, the SAR values for the proposed antenna were as follows: 0.0066 W/kg at 0.915 GHz, 0.0095 W/kg at 1.4 GHz, and 0.0140 W/kg at 2.45 GHz. These values are well below the safety

TABLE III
LINK BUDGET PARAMETERS ANALYSIS

Signal power			
Varaibale	Parameter	value	Unit
Transmitter Side			
P_t	Transmitted power	-16	dBm
f	Frequency	915, 1400, 2450	MHz
G_t	Antenna gain	-32.4, -27.94, -19.8	dBi
Propagation medium			
L_f	Path loss	Variable	dB
Receiver Side			
G_r	Receiver antenna gain	2	dBi
Noise power			
N_o	Noise power density	-203.93	dBm/Hz
T	Temperature	273	Kelvin
K	Boltzmann constant	1.38×10^{-23}	J/K
Signal quality			
B_r	Bit rate	various	Mbps
BER	Bit error rate	1×10^{-5}	-
E_b/N_o	Ideal PSK	9.6	dB
G_c	Coding gain	0	dB
G_d	Fixing deterioration	2.5	dB

limits of 1.6 W/kg and 2 W/kg, demonstrating that the antenna's SAR levels are within acceptable standards for safety within the human body.

E. Link Budget Analysis

A link budget analysis is performed to assess the communication link between the implantable antenna and the external device. This involves computing the link margin (LM), (difference between received power (R_p) and the required minimum receiver sensitivity (S_p)). The margin value must exceed 0 dB for successful signal reception. However, a minimum link margin of 20 dB is chosen to ensure reliable communication. This study assumes 10 Mbps as bit rate (B_r) to understand its impact on the link margin, using Equation (2) [32].

$$LM[dB] = R_p - S_p \quad \text{, where } R_p > S_p \tag{2}$$

Received power can be calculated using Friis Equation (3) [33], which focuses on three components: power, gain, and losses on all signal paths that it may go through.

$$R_p[dB] = P_t + G_t + G_r - L_f - L_p - N_o \tag{3}$$

$$S_p = (E_b/N_o) + 10\log_{10}(B_r) - G_c + G_d \tag{4}$$

where

$$L_f[\text{dB}] = 10\log_{10}\left(\frac{4\pi d}{\lambda}\right)^2 \tag{5}$$

and

$$N_o = 10\log_{10}(KT_o) \tag{6}$$

where, L_p is the polarization loss factor. The values of L_f and L_p are calculated based on equations in [34]. In the calculations for the link budget, the proposed antenna is treated as the transmitter, and an ideal half-wavelength dipole antenna is chosen as the receiver antenna, (a gain of 2 dBi). The distance between them is denoted by d. [35].

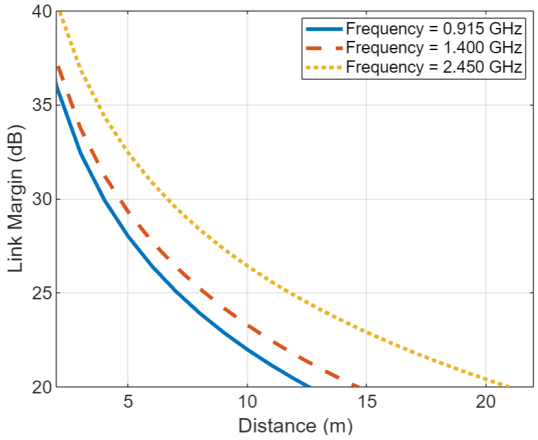

Fig. 9. Link margin at 10 Mbps across different frequency bands.

TABLE IV
COMPARISON OF THE PROPOSED ANTENNA WITH PREVIOUS DESIGNS

Ref.	Frequency (GHz)	Volume (mm^3)	FBW (%)	Gain (dBi)	Size $(\lambda_g)^3$	SAR (W/kg) 1 - g	SAR (W/kg) 10 - g
[5]	0.433	240	74.1	-23.19	3.02×10^{-1}	177.1	-
[6]	2.4	121.9	21.5	-33	2×10^{-3}	486	90
[7]	2.45	99.7	20.5	-26.4	1.76×10^{-3}	712.1	-
[8]	2.45	70.4	88.6	-16.5	1.25×10^{-3}	269	-
[9]	2.4	63.8	16.12	-37.3	1.06×10^{-3}	856.4	-
[10]	2.45	59.5	40.8	-16	1.11×10^{-4}	330.4	39.9
[11]	0.915	28.85	84	-30.2	2.66×10^{-5}	796.1	64.1
[12]	2.4	39.3	14.9	-20.75	1.31×10^{-4}	568.2	84.6
[13]	2.45	24	8.57	-22.8	4.26×10^{-4}	807.3	102.4
[37]	0.915	18.3	84.91	-30.4	3.4×10^{-6}	-	-
[14]	2.45	17.15	9	-18.2	3.04×10^{-4}	305	81.7
T.W	1.4	9.44	138	-27.94	1.39×10^{-6}	378.1	40.3

T.W = This work

The input power for transmission is set at -16 dBm (as discussed in Section III.D) [36], while considering transmitting gains of -32.4, -27.94, and -19.8 dBi at 0.915 GHz, 1.4 GHz, and 2.45 GHz, respectively. Losses arising from polarization and impedance mismatches are not considered in this analysis. The antenna is sufficiently matched, which minimizes impedance mismatch losses. All other parameter values involved in link margin calculations are shown in Table III. In Fig. 9, with a bit rate of 10 Mbps, the antenna covers distances of 12, 14, and 21 meters at frequencies of 0.915, 1.4, and 2.45 GHz, respectively. For typical leadless pacemaker use, the external receiver is placed 1-2 meters from the patient, ensuring reliable biotelemetry. Although there are higher propagation losses at 2.45 GHz, its superior gain of -19.8 dBi, compared to -32.4 dBi at 0.915 GHz and -27.94 dBi at 1.4 GHz, results in better overall coverage.

This antenna is compared with recent designs, as illustrated in Table IV. It features the smallest guided wavelength size and achieves the largest FBW among recently reported implantable antennas.

Thus, making it suitable for pacemaker devices, operating in lossy heterogeneous heart tissue.

IV. Conclusion

A compact and wide-bandwidth implantable antenna has been designed, simulated, and experimentally validated for next-generation LCPs. The remarkable performance has been achieved through the incorporation of innovative design techniques, including expanded slots in the ground plane, a U-shaped slot, additional rectangular slots on the radiating patch, and an inductive shorting pin. As a result, the proposed antenna occupies a compact volume of 9.44 mm^3, and achieves a broad bandwidth of 3.39 GHz (FBW = 138%). Moreover, the antenna shows gains of -32.4, -27.94, and -19.8 dBi at 0.915 GHz, 1.4 GHz, and 2.45 GHz, respectively. The simulation was performed in the heart of a human phantom, and measurements were carried out inside minced pork meat. Both simulation and measured results confirm stable impedance matching, wide bandwidth, high gains, and stable radiation patterns. SAR values are below IEEE guidelines, which highlight its suitability for LCPs.

References

[1] S. M. Asif, J. W. Hansen, A. Iftikhar, D. L. Ewert, and B. D. Braaten, "Computation of available rf power inside the body and path loss using in vivo experiments," *IET Microwaves, Antennas & Propagation*, vol. 13, no. 1, pp. 122–126, 2019.

[2] M. Rav Acha, E. Soifer, and T. Hasin, "Cardiac implantable electronic miniaturized and micro devices," *Micromachines*, vol. 11, no. 10, p. 902, 2020.

[3] N. E. Beurskens, K. T. Breeman, K. J. Dasselaar, A. C. Meijer, A.-F. B. Quast, F. V. Tjong, and R. E. Knops, "Leadless cardiac pacing systems: current status and future prospects," *Expert review of medical devices*, vol. 16, no. 11, pp. 923–930, 2019.

[4] M. Fallahpour and R. Zoughi, "Antenna miniaturization techniques: A review of topology-and material-based methods," *IEEE Antennas and Propagation Magazine*, vol. 60, no. 1, pp. 38–50, 2017.

[5] H. Li, B. Wang, L. Guo, and J. Xiong, "Efficient and wideband implantable antenna based on magnetic structures," *IEEE Transactions on Antennas and Propagation*, vol. 67, no. 12, pp. 7242–7251, 2019.

[6] Z. Xia, H. Li, Z. Lee, S. Xiao, W. Shao, X. Ding, *et al.*, "A wideband circularly polarized implantable patch antenna for ism band biomedical applications," *IEEE Transactions on Antennas and Propagation*, vol. 68, no. 3, pp. 2399–2404, 2020.

[7] W. Cui, R. Liu, L. Wang, M. Wang, H. Zheng, and E. Li, "Design of wideband implantable antenna for wireless capsule endoscope system," *IEEE Antennas and Wireless Propagation Letters*, vol. 18, no. 12, pp. 2706–2710, 2019.

[8] S. Bhattacharjee, S. Maity, S. R. Bhadra Chaudhuri, and M. Mitra, "Metamaterial-inspired wideband biocompatible antenna for implantable applications," *IET Microwaves, Antennas & Propagation*, vol. 12, no. 11, pp. 1799–1805, 2018.

[9] R. Liu, K. Zhang, Z. Li, W. Cui, W. Liang, M. Wang, C. Fan, H. Zheng, and E. Li, "A wideband circular polarization implantable antenna for health monitor microsystem," *IEEE Antennas and Wireless Propagation Letters*, vol. 20, no. 5, pp. 848–852, 2021.

[10] A. Basir, A. Bouazizi, M. Zada, A. Iqbal, S. Ullah, and U. Naeem, "A dual-band implantable antenna with wide-band characteristics at mics and ism bands," *microwave and optical technology letters*, vol. 60, no. 12, pp. 2944–2949, 2018.

[11] A. Basir and H. Yoo, "A stable impedance-matched ultrawideband antenna system mitigating detuning effects for multiple biotelemetric applications," *IEEE Transactions on Antennas and Propagation*, vol. 67, no. 5, pp. 3416–3421, 2019.

[12] S. Hout and J.-Y. Chung, "Design and characterization of a miniaturized implantable antenna in a seven-layer brain phantom," *IEEE Access*, vol. 7, pp. 162062–162069, 2019.

[13] S. A. A. Shah and H. Yoo, "Scalp-implantable antenna systems for intracranial pressure monitoring," *IEEE Transactions on Antennas and Propagation*, vol. 66, no. 4, pp. 2170–2173, 2018.

[14] I. A. Shah, M. Zada, and H. Yoo, "Design and analysis of a compact-sized multiband spiral-shaped implantable antenna for scalp implantable and leadless pacemaker systems," *IEEE Transactions on Antennas and Propagation*, vol. 67, no. 6, pp. 4230–4234, 2019.

[15] M. Zada, I. A. Shah, A. Basir, and H. Yoo, "Ultra-compact implantable antenna with enhanced performance for leadless cardiac pacemaker system," *IEEE Transactions on antennas and propagation*, vol. 69, no. 2, pp. 1152–1157, 2020.

[16] F. Faisal, M. Zada, H. Yoo, I. B. Mabrouk, M. Chaker, and T. Djerafi, "An ultra-miniaturized antenna with ultra-wide bandwidth for future cardiac leadless pacemaker," *IEEE Transactions on Antennas and Propagation*, vol. 70, no. 7, pp. 5923–5928, 2022.

[17] S. Shamim, M. S. Uddin, M. R. Hasan, and M. Samad, "Design and implementation of miniaturized wideband microstrip patch antenna for high-speed terahertz applications," *Journal of Computational Electronics*, vol. 20, pp. 604–610, 2021.

[18] C. E. Shannon, "A mathematical theory of communication," *The Bell system technical journal*, vol. 27, no. 3, pp. 379–423, 1948.

[19] K.-L. Wong, *Compact Dual-Frequency and Dual-Polarized Microstrip Antennas*, ch. 4, pp. 115–121. New York, USA: John Wiley & Sons Inc., 2002.

[20] T. Huynh and K.-F. Lee, "Single-layer single-patch wideband microstrip antenna," *Electronics letters*, vol. 31, no. 16, pp. 1310–1312, 1995.

[21] R. B. Simorangkir, Y. Yang, L. Matekovits, and K. P. Esselle, "Dual-band dual-mode textile antenna on pdms substrate for body-centric communications," *IEEE Antennas and Wireless Propagation Letters*, vol. 16, pp. 677–680, 2016.

[22] S.-C. Pan and K.-L. Wong, "Dual-frequency triangular microstrip antenna with a shorting pin," *IEEE Transactions on Antennas and Propagation*, vol. 45, no. 12, pp. 1889–1891, 1997.

[23] K.-L. Wong and W.-H. Hsu, "A broad-band rectangular patch antenna with a pair of wide slits," *IEEE Transactions on Antennas and Propagation*, vol. 49, no. 9, pp. 1345–1347, 2001.

[24] E. Abdo-Sanchez, J. E. Page, T. M. Martin-Guerrero, J. Esteban, and C. Camacho-Penalosa, "Planar broadband slot radiating element based on microstrip-slot coupling for series-fed arrays," *IEEE Transactions on Antennas and Propagation*, vol. 60, no. 12, pp. 6037–6042, 2012.

[25] A. A. Kishk, A. W. Glisson, and G. P. Junker, "Bandwidth enhancement for split ground plane microstrip patch antennas," *IEEE Transactions on Antennas and Propagation*, vol. 51, no. 3, pp. 578–585, 2003.

[26] R. De Silva, I. Kitulwatte, D. Priyanath, M. Gunathilake, T. Senanayake, and M. Kumari, "Study on heart measurements of the people between the age 20-40 years present to the teaching hospital colombo north–post mortem study," 2021.

[27] "Niremf - national interuniversity consortium for telecommunications (cnit)." Accessed on October 26, 2023.

[28] N. K. Mallat and A. Iqbal, "Substrate integrated waveguide-based simultaneous transmit and receive antenna for full-duplex wearable devices," *International Journal of RF and Microwave Computer-Aided Engineering*, vol. 32, no. 7, p. e23188, 2022.

[29] D. Nikolayev, W. Joseph, M. Zhadobov, R. Sauleau, and L. Martens, "Optimal radiation of body-implanted capsules," *Physical review letters*, vol. 122, no. 10, p. 108101, 2019.

[30] M. M. Soliman, M. E. Chowdhury, A. Khandakar, M. T. Islam, Y. Qiblawey, F. Musharavati, and E. Zal Nezhad, "Review on medical implantable antenna technology and imminent research challenges," *Sensors*, vol. 21, no. 9, p. 3163, 2021.

[31] F. Rules, "Regulations 47 cfr part 95," *Subparts E (95.601-95.673) and I (95.1201-95.1219) Personal Radio Services*, 2002.

[32] A. Basir, M. Zada, Y. Cho, and H. Yoo, "A dual-circular-polarized endoscopic antenna with wideband characteristics and wireless biotelemetric link characterization," *IEEE Transactions on Antennas and Propagation*, vol. 68, no. 10, pp. 6953–6963, 2020.

[33] C. A. Balanis, *Antenna theory: analysis and design*. John wiley & sons, 2016.

[34] A. Iqbal, M. Al-Hasan, I. B. Mabrouk, and T. A. Denidni, "Self-quadruplexing antenna for scalp-implantable devices," *IEEE Transactions on Antennas and Propagation*, vol. 72, pp. 2252–2260, March 2024.

[35] J. B. Andersen and A. Frandsen, "Absorption efficiency of receiving antennas," *IEEE Transactions on Antennas and Propagation*, vol. 53, no. 9, pp. 2843–289, 2005.

[36] F. Faisal, M. Zada, A. Ejaz, Y. Amin, S. Ullah, and H. Yoo, "A miniaturized dual-band implantable antenna system for medical applications," *IEEE Transactions on Antennas and Propagation*, vol. 68, no. 2, pp. 1161–1165, 2019.

[37] L. Chang, A. Iqbal, A. Basir, R. B. Simorangkir, and I. B. Mabrouk, "Conformal mimo ultra-wideband antenna design for high-speed wireless telemetry in capsule endoscopy systems," *IEEE Transactions on Antennas and Propagation*, 2024.